The Astrophysical Journal, 900:190 (13pp), 2020 September 10 https://doi.org/10.3847/1538-4357/abaab8

Resolving Decades of Periodic Spirals from the Wolf–Rayet Dust Factory WR 112

Ryan M. Lau[1], Matthew J. Hankins[2], Yinuo Han[3], Izumi Endo[4], Anthony F. J. Moffat[5,6], Michael E. Ressler[7], Itsuki Sakon[4], Joel Sanchez-Bermudez[8], Anthony Soulain[3], Ian R. Stevens[9], Peter G. Tuthill[3], and Peredur M. Williams[10]
[1] Institute of Space & Astronautical Science, Japan Aerospace Exploration Agency, 3-1-1 Yoshinodai, Chuo-ku, Sagamihara, Kanagawa 252-5210, Japan
ryanlau@ir.isas.jaxa.jp
[2] Division of Physics, Mathematics, and Astronomy, California Institute of Technology, Pasadena, CA 91125, USA
[3] Sydney Institute of Astronomy (SIfA), School of Physics, The University of Sydney, NSW 2006, Australia
[4] Department of Astronomy, School of Science, University of Tokyo, 7-3-1 Hongo, Bunkyo-ku, Tokyo 113-0033, Japan
[5] Département de physique, Université de Montréal, C.P. 6128, succ. Centre-ville, Montréal, QC H3C 3J7, Canada
[6] Centre de Recherche en Astrophysique du Québec, Canada
[7] Jet Propulsion Laboratory, California Institute of Technology, 4800 Oak Grove Dr., Pasadena, CA 91109, USA
[8] Instituto de Astronomía, Universidad Nacional Autónoma de México, Apdo. Postal 70264, Ciudad de México 04510, Mexico
[9] School of Physics and Astronomy, University of Birmingham, Edgbaston, Birmingham B15 2TT, UK
[10] Institute for Astronomy, University of Edinburgh, Royal Observatory, Edinburgh EH9 3HJ, UK
Received 2020 June 11; revised 2020 July 22; accepted 2020 July 22; published 2020 September 15

Abstract

WR 112 is a dust-forming carbon-rich Wolf–Rayet (WC) binary with a dusty circumstellar nebula that exhibits a complex asymmetric morphology, which traces the orbital motion and dust formation in the colliding winds of the central binary. Unraveling the complicated circumstellar dust emission around WR 112 therefore provides an opportunity to understand the dust formation process in colliding-wind WC binaries. In this work, we present a multi-epoch analysis of the circumstellar dust around WR 112 using seven high spatial resolution (FWHM $\sim 0\farcs3$–$0\farcs4$) *N*-band ($\lambda \sim 12\ \mu$m) imaging observations spanning almost 20 yr and that includes images obtained from Subaru/COMICS in 2019 October. In contrast to previous interpretations of a face-on spiral morphology, we observe clear evidence of proper motion of the circumstellar dust around WR 112 consistent with a nearly edge-on spiral with a $\theta_s = 55°$ half-opening angle and a ~20 yr period. The revised near edge-on geometry of WR 112 reconciles previous observations of highly variable nonthermal radio emission that was inconsistent with a face-on geometry. We estimate a revised distance to WR 112 of $d = 3.39^{+0.89}_{-0.84}$ kpc based on the observed dust expansion rate and a spectroscopically derived WC terminal wind velocity of $v_\infty = 1230 \pm 260\ \mathrm{km\ s^{-1}}$. With the newly derived WR 112 parameters, we fit optically thin dust spectral energy distribution models and determine a dust production rate of $\dot{M}_\mathrm{d} = 2.7^{+1.0}_{-1.3} \times 10^{-6}\ M_\odot\ \mathrm{yr}^{-1}$, which demonstrates that WR 112 is one of the most prolific dust-making WC systems known.

Unified Astronomy Thesaurus concepts: Circumstellar dust (236); WC stars (1793); Dust shells (414); Dust nebulae (413); Binary stars (154)

Supporting material: animation

1. Introduction

Classical Wolf–Rayet (WR) stars are descendants of massive O-type stars that exhibit fast winds ($\gtrsim$1000 km s^{-1}), hot photospheres ($T_* \gtrsim 40{,}000$ K), and high luminosities ($L_* \sim 10^5\ L_\odot$; Crowther 2007). Despite their extreme environments, a subset of carbon-rich WR (WC) stars have been observed to actively form dust (Gehrz & Hackwell 1974; Williams et al. 1987). These dust-forming WC stars, also referred to as "dustars" (Marchenko & Moffat 2007), can be prolific sources of dust with production rates ranging from $\dot{M}_\mathrm{d} \sim 10^{-10}$–$10^{-6}\ M_\odot\ \mathrm{yr}^{-1}$ (Zubko 1998; Lau et al. 2020). Due to their large dust output and the short evolutionary timescale associated with the onset of the WR phase ($\lesssim$1 Myr), WC dustars are likely to be early and significant sources of dust (Lau et al. 2020). However, many open questions persist about the nature of dust formation in these systems.

The presence of a binary companion is believed to be a key factor for dust formation in the hostile environment around WC dustars. The strong wind from the WC star interacts and collides with the weaker wind from an OB-star companion, which creates a dense shock front that cools, forms dust, and streams away from the central binary (Williams et al. 1990; Usov 1991). Due to the orbital motion of the central binary, newly formed dust propagates radially outward in different directions corresponding to the orbital phase of the system. Observational evidence of this phenomenon is clearly demonstrated in the changing orientation of the dusty "pinwheel" revealed in WR 104 by Tuthill et al. (1999). The morphology and proper motion of the WC dustar nebulae therefore trace the colliding-wind dust formation and orbital configuration of the central binary.

The analysis of mid-infrared (IR) imaging observations that are capable of resolving the nebulae around Galactic WC dustars has recently revealed gaps in our understanding of their dust formation process. For example, the newly discovered WC dustar known as Apep (2XMM J160050.7514245; Callingham et al. 2019) exhibits inconsistent dynamics between the dust expansion and the WC wind velocities. An even more long-standing mystery is the nature of the apparent broken pinwheel nebulae surrounding the WC dustar WR 112 (CRL 2104; Cohen & Kuhi 1976; Marchenko et al. 2002; Lau et al. 2017).

The WR star in WR 112 was initially classified as a WC8 star by Cohen & Kuhi (1976), who attributed the relative weakness of the 4650 Å C III–IV feature to dilution by a luminous, blue companion. However, no stellar absorption lines were observed from the companion. Massey & Conti (1983)

reclassified WR 112 as a WC9 star based on optical spectroscopy showing the presence of C II lines and a strong 5696 Å C III feature with a weaker 5802,12 Å C IV feature. The stellar subtype is therefore disputed, but we will argue in favor of the initial WC8 classification based the quantitative spectral classification criteria for WC stars by Crowther et al. (1998).

Although the companion star in WR 112 has not been directly observed, nonthermal radio emission from this system demonstrates that it hosts a colliding-wind binary (Leitherer et al. 1997; Chapman et al. 1999; Monnier et al. 2002). However, its highly variable nonthermal radio emission and the complex dust morphology of its surrounding nebula complicate our understanding of the dust formation and binary orbital parameters in this system. This issue is compounded by the conflicting interpretations of the dust morphology and dust proper motion (Marchenko et al. 2002; Monnier et al. 2007; Lau et al. 2017).

In their analysis of a single-epoch *N*-band ($\lambda \sim 12$ μm) image of WR 112, Marchenko et al. (2002) initially interpreted the WR 112 dust morphology as a near face-on pinwheel spiral similar to that of WR104 (Tuthill et al. 2008). However, this model is unable to account for several dust features that deviate from the face-on morphology. Keck aperture-masking observations by Monnier et al. (2007) probed dust emission features down to ~20 mas and demonstrated that the central region of WR 112 exhibits no obvious spiral structure, but rather a "horseshoe" structure with two spurs from the central source extending north. These results suggest a morphology more consistent with an edge-on, as opposed to a face-on, viewing angle. An edge-on interpretation for WR 112 was initially hypothesized by Monnier et al. (2002) to explain its highly variable nonthermal radio emission. Most recently, Lau et al. (2017) reinterpreted the circumstellar nebula around WR 112 as a consecutive series of "stagnant" dust shells exhibiting no proper motion. However, Lau et al. (2017) based their interpretation primarily on two *N*-band observations taken ~9 yr apart, and one of the observations was assumed to be rotated by 180°.

In this work, we present new *N*-band ($\lambda \sim 12$ μm) imaging data of WR 112 with the Cooled Mid-infrared Camera and Spectrometer (COMICS) on the Subaru Telescope taken in 2019 October and conduct a multi-epoch proper motion and morphological analysis of high spatial resolution *N*-band imaging observations taken over almost 20 yr. We revise the morphological interpretation of the spiral geometry of the WR 112 nebula to reconcile the inconsistencies of previous observational IR studies. With the new results from our geometric spiral model, we revisit the distance estimate to WR 112 and its dust production properties. We also describe how our revised WR 112 geometry can explain the observed nonthermal radio variability. Lastly, we discuss how WR 112's revised orbital and dust production properties compare it to the population of known WC dustars.

2. Observations and Archival Data

2.1. Subaru/COMICS Mid-infrared Imaging

Mid-IR imaging observations of WR 112 (J2000 R.A. 18:16:33.49, decl.−18:58:42.3; Cutri et al. 2003) were obtained using the COMICS instrument (Kataza et al. 2000; Okamoto et al. 2003) on the Cassegrain focus of the Subaru Telescope with the N11.7 filter ($\lambda = 11.7$ μm, $\Delta\lambda = 1.0$ μm) on 2019 October 12

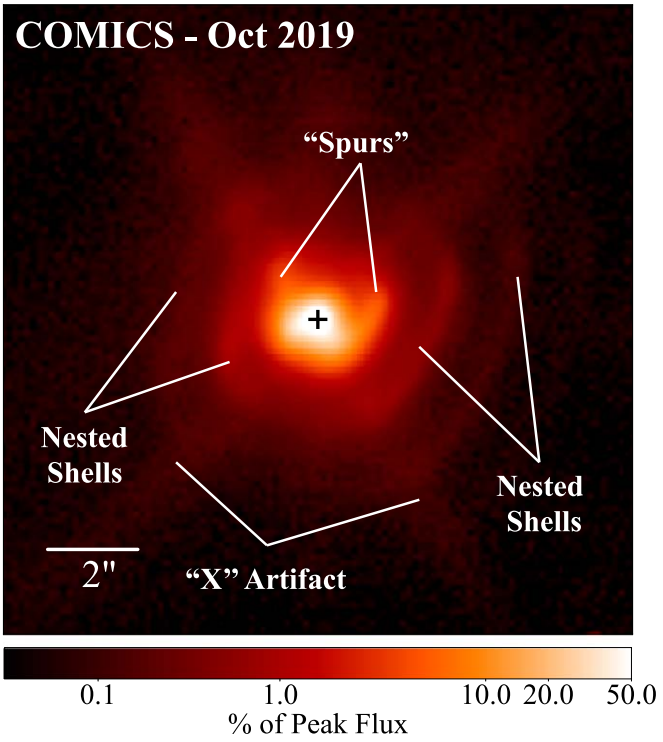

Figure 1. Logarithmic stretch from 0.01% to 50% of peak flux density of the newly obtained Subaru/COMICS N11.7 image of WR 112 overlaid with the features corresponding to the "spurs" and the nested shell-like emission. The "X"-shaped artifact due to diffraction by the secondary mirror support struts is also labeled. North is up and east is left.

(Figure 1). Individual 200 s exposures were performed using a perpendicular chopping and nodding pattern with a 20″ amplitude. The total integration time on WR 112 was 20.1 min. The pixel scale of the detector is 0.″13 pixel^{-1}.

Gamma Aql was used as the photometric and point-spread function (PSF) reference from the list of mid-IR standards in Cohen et al. (1999). The measured FWHM of the calibrator was ~0.″33, which is consistent with near diffraction-limited performance at 11.7 μm (0.″29).

The data reduction was carried out using COMICS Reduction Software and IRAF. The chopping and nodding pair subtraction was employed to cancel out the background radiation and to reduce a residual pattern from the chop subtraction. Flat fielding was achieved using a self-sky-flat made from each image. A conversion factor for flux density calibration was calculated using the reduced images of the standard star and its photometric data from Cohen et al. (1999). The total observed N11.7 flux density from WR 112 is 143 ± 14 Jy, where we assume a photometric calibration uncertainty of ~10%. This is consistent with *N*-band photometry from previous space- and ground-based observations of WR 112 (Lau et al. 2017).

There are two artifacts present in the COMICS image of WR 112 due to its brightness. The most prominent artifact is the "X"-shaped emission centered on WR 112 (Figure 1), which arises due to diffraction by the secondary mirror support struts (see Murakawa et al. 2004). The second, less-prominent artifact is the "ringing" that extends from the center of WR 112 in the row-direction due to cross-talk along the readout channels. The cross-talk artifact is mitigated by the COMICS data reduction routines. As the morphology of the circumstellar dust emission from WR 112 is distinguishable from the

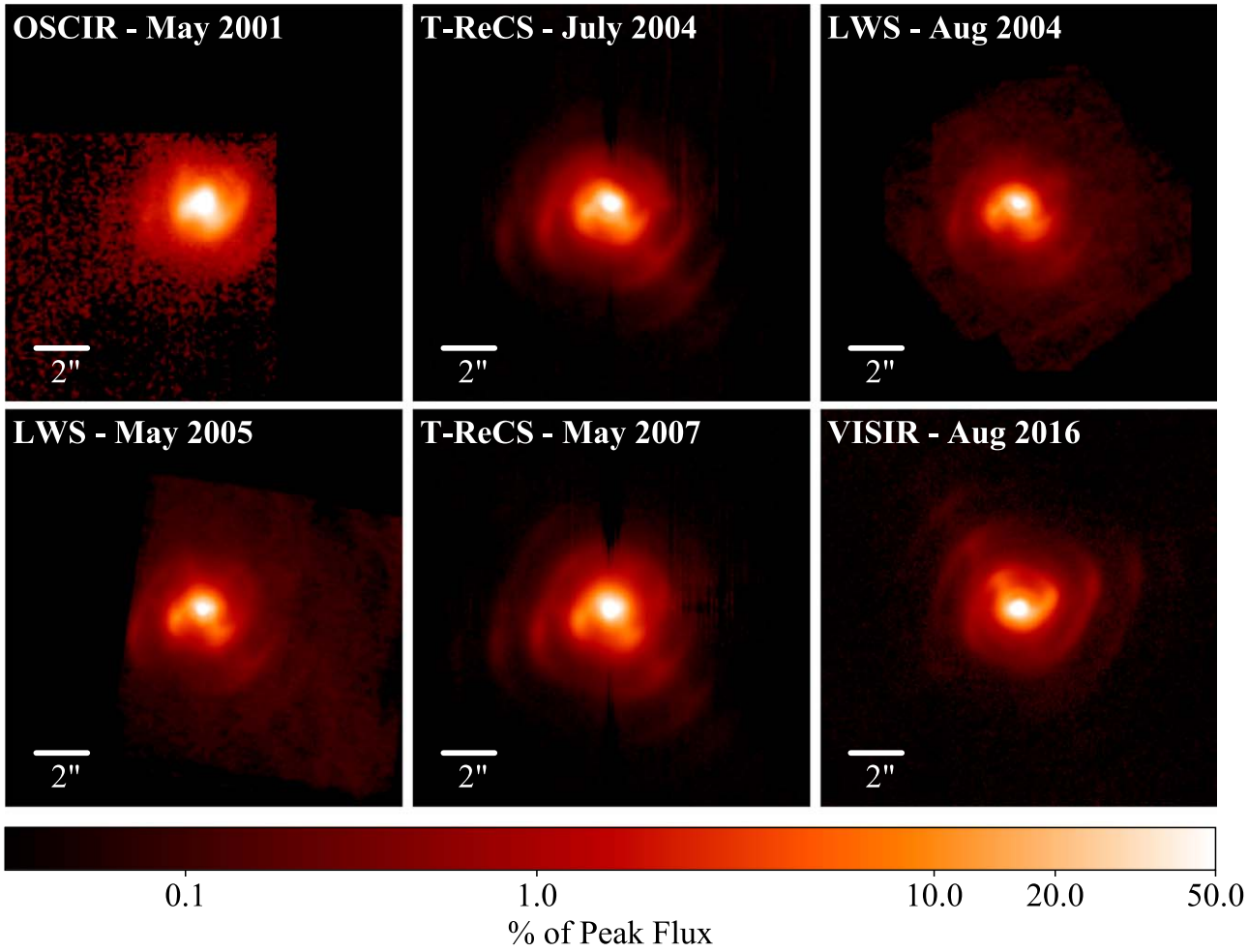

Figure 2. Logarithmic stretch from 0.01% to 50% of peak flux density of six previous *N*-band images of WR 112 taken by Gemini North/OSCIR, Gemini South/T-ReCS, Keck I/LWS, and VLT/VISIR. North is up and east is left in all panels.

structure of the X-shaped artifact, and to preserve the signal-to-noise of the extended nebulosity, the analysis on the image is carried out without correction for this artifact.

Hereafter, we refer to the Subaru/COMICS observations as S2019.

2.2. Archival Mid-infrared Imaging

Within the past 20 yr, WR 112 has been observed with *N*-band imaging in at least six different epochs in addition to S2019 by the following instruments: the Observatory Spectrometer and Camera for the Infrared (OSCIR) at Gemini North on 2001 May 7 (PID GN-2001A-C-16), the Thermal-Region Camera Spectrograph (T-ReCS; De Buizer & Fisher 2005) at Gemini South on 2004 July 8 (PID GS-2004A-Q-63; PI A. Moffat) and 2007 May 7 (PID GS-2007A-Q-38; PI J. Monnier), the Long Wavelength Spectrometer (LWS; Jones & Puetter 1993) on the Keck I Telescope on 2004 August 31 (PID U18LS; PI Townes) and on 2005 May 26 (PID U71LSN; PI Townes), and the Very Large Telescope (VLT) spectrometer and imager for the mid-infrared (VISIR; Lagage et al. 2004) on 2016 August 9 (PID 097.D-0707(A); PI R. Lau). These six images are shown in Figure 2, and information on all seven of the *N*-band observations is summarized in Table 1. The filters have different passbands but are sufficiently close in wavelength to probe the same thermal dust emission components from the WR 112 nebula. This is apparent in the identical dust emission morphologies exhibited by WR 112 in 8.6, 13.04, and 19.5 μm imaging by VISIR (Lau et al. 2017).

Hereafter, we refer to the 2001 Gemini North/OSCIR, 2004 Gemini South/T-ReCS, 2004 Keck I/LWS, 2005 Keck I/LWS, 2007 Gemini South/T-ReCS, and 2016 VLT/VISIR observations as G2001, G2004, K2004, K2005, G2007, and V2016, respectively.

Both K2004 and K2005 images are presented for the first time in this work. The K2004 and K2005 images were obtained in a nonstandard observing mode with varying parallactic angles optimized for an interferometric observing mode, which was the primary focus of the WR 112 program with Keck I/LWS. Standard chopping and dithering were utilized to subtract background emission and mitigate the effects of bad pixels, respectively. The reduced K2004 and K2005 images were obtained by averaging the chop-subtracted, centroid-aligned, and rotation-corrected individual exposures.

G2001 and G2004 data were published in Marchenko et al. (2002) and Marchenko & Moffat (2007), respectively, and G2007 and V2016 data were presented in Lau et al. (2017). The G2004 and G2007 images were affected by a bright source artifact known as the "hammer effect"[11] that causes negative regions that extend vertically and horizontally from the bright

[11] See https://www.gemini.edu/sciops/instruments/midir-resources/data-reduction/data-format-and-features.

Table 1
Summary of WR 112 *N*-band Observations

Observatory	Instrument	Obs. Date	Filter Name	λ_c and $\Delta\lambda(\mu m)$	Abbreviation
Gemini North	OSCIR	2001 May 7	12.5	12.49, 1.16	G2001
Gemini South	T-ReCS	2004 Jul 8	Si-6	12.33, 1.18	G2004
Keck I	LWS	2004 Aug 31	10.7	10.7, 1.6	K2004
Keck I	LWS	2005 May 26	10.7	10.7, 1.6	K2005
Gemini South	T-ReCS	2007 May 7	Si-5	11.66, 1.13	G2007
VLT	VISIR	2016 Aug 9	NEII_2	13.04, 0.20	V2016
Subaru	COMICS	2019 Oct 12	N11.7	11.7, 1.0	S2019

Note. λ_c and $\Delta\lambda$ correspond to the central wavelength and bandwidth of each filter.

central core. This effect is mitigated by a median-filter subtraction across the image. Although dark vertical bands are still present around the bright central source in the G2004 and G2007 images (Figure 2), the overall dust emission morphology is readily discernible.

All seven *N*-band observations, which were obtained on 8–10 m class telescopes, are Nyquist sampled and achieve near diffraction-limited angular resolutions of ∼0.″3–0.″4. OSCIR, T-ReCS, LWS, VISIR, and COMICS use different imager pixel scales of 0.089, 0.09, 0.083,[12] 0.045, and 0.″13 pixel^{-1}, respectively. The OSCIR, T-ReCS, LWS, and COMICS images were therefore up-sampled to match the 0.″045 pixel^{-1} scale of the VISIR image. After resampling to the 0.″045 pixel^{-1} scale, the images were aligned with the centroid of the bright central core fit by a 2D Gaussian.

2.3. Archival Mid-infrared Spectroscopy

Archival medium resolution ($R \approx 250$–600) 2.2–40 μm spectra of WR 112 were taken by the Short Wavelength Spectrometer (SWS; de Graauw et al. 1996) on the Infrared Space Observatory (ISO; Kessler et al. 1996) and were obtained in the WRSTARS program (PI van der Hucht; van der Hucht et al. 1996) on 1996 February 27. The reduced "sws" file of the SWS spectrum of WR 112 was obtained from the database of SWS spectra processed and hosted by Sloan et al. (2003).[13] The WR 112 spectrum was smoothed by a median filter with a 51-element kernel.

The WR 112 "pws" file, which shows the spectrum prior to segment-to-segment normalization, did not exhibit significant segment discontinuities greater than ∼10%. However, due to larger flux density uncertainties beyond 27.5 μm, only the 2.2–27.5 μm data were used.

This ISO/SWS spectrum of WR 112 has been previously presented and/or analyzed by van der Hucht et al. (1996), Chiar & Tielens (2001, 2006), Lau et al. (2017), and Marchenko & Moffat (2017).

2.4. Optical Spectroscopy and WC8 Spectral Subtype Confirmation

WR 112 was observed with the Intermediate-dispersion Spectrograph and Imaging System (ISIS) on the William Herschel Telescope (WHT) in the Service Observing program on 1999 July 30 using the R300B grating, which gave a spectral resolution of ∼5 Å for a 1.″2 slit. The observation was composed of five integrations of 1500 s, interspersed with observations of an argon lamp for wavelength calibration. Flat fields were observed at the beginning of the night. The data were reduced using the FIGARO package (Shortridge 1993) within the UK Starlink system (Currie et al. 2014).

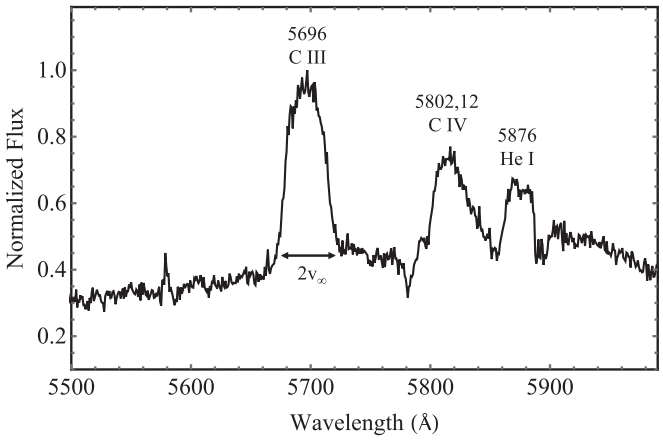

Figure 3. Optical WHT/ISIS spectrum of WR 112 taken on 1999 July 30 and normalized to the peak flux density of the 5696 Å C III emission line.

The spectrum (Figure 3) shows prominent carbon and helium emission lines consistent with a late-type WC star. No hydrogen or helium absorption lines indicating an OB companion are present. However, a luminous line-of-sight "neighbor" is located 942 mas to the SW of WR 112 and is 2.81 mag brighter than WR 112 in the F439W filter taken by the Wide Field and Planetary Camera II on the Hubble Space Telescope (Wallace et al. 2002). This neighbor unfortunately falls in the aperture used for the WHT/ISIS spectrum of WR 112 and is also included in the aperture used by earlier spectroscopy by Cohen & Kuhi (1976) and Massey & Conti (1983). The neighbor dominates the spectrum in the blue, diluting not only the WC emission lines but also any absorption lines from the expected OB companion.

The prominent 5696 Å C III line is expected to form in the outer region of the WC wind where it has attained its terminal velocity. The WC wind terminal velocity can then be estimated from the full width at zero intensity (FWZI) of the C III line, where FWZI $\approx 2v_\infty$. The measured terminal velocity is $v_\infty = 1230 \pm 260$ km s^{-1}.

The primary quantitative WC subtype classification criteria from Crowther et al. (1998) is the equivalent width ratio of the 5802,12 Å C IV and 5696 Å C III features. For WC8 stars, Crowther et al. (1998) determine that $\mathrm{Log}(W_\lambda\ (\mathrm{C\ IV})/W_\lambda\ (\mathrm{C\ III})) = -0.3$ to $+0.1$. The WHT/ISIS spectrum of WR 112 provides a line ratio of $\mathrm{Log}(W_\lambda\ (\mathrm{C\ IV})/W_\lambda\ (\mathrm{C\ III})) = -0.11$, which is consistent with a WC8 classification based on the

[12] The official LWS pixel scale is 0.″085 pixel^{-1}, but revised calibration of the K2004 and K2005 images indicated a pixel scale closer to 0.″083 pixel^{-1}.
[13] https://users.physics.unc.edu/~gcsloan/library/swsatlas/atlas.html

Crowther et al. (1998) criteria. This corroborates WR 112's initial WC8 classification by Cohen & Kuhi (1976) rather than the reclassification as WC9 by Massey & Conti (1983).

3. Results and Analysis

3.1. Dust Morphology and Proper Motion

The circumstellar dust around WR 112 exhibits a complex morphology with nested, asymmetric shell-like features and two "spurs" extending from the bright central point source (Figure 1). Despite the lack of azimuthal symmetry, the successive shells exhibit identical features in the radial direction, which suggests the nested features are related through a periodic formation mechanism.

The WR 112 nebula shows distinct morphological changes over the 18 yr span of the *N*-band imaging observations. Figure 2 demonstrates the evolving circumstellar dust morphology that is most apparent when comparing the bright, central $\lesssim 1\farcs5$ regions in the G2007 and V2016 images. The central regions of the S2019 (Figure 1) and V2016 images show the two spurs extending to the north, whereas the spurs are oriented to the south in the G2004, K2004, K2005 and G2007 images. These central regions show subtle differences between the images taken $\lesssim 3$ yr apart. For example, the central morphology in S2019 exhibits a "W"-like appearance, which slightly deviates from the "ν"-shaped morphology in the V2016 images. The central region of the G2001 image also exhibits a "W"-shaped appearance, which was addressed explicitly by Marchenko et al. (2002).

The G2004, K2004, K2005, G2007, V2016, and S2019 observations exhibit identical $\sim 1\farcs5$ spacings between successive, nested shells located $\gtrsim 2''$ from the center. These images reveal emission from at least two dust shells to beyond the two central spurs to the east and west (Figures 1 and 2). Only the first nested dust shell was detected in the G2001 image due to its lower signal-to-noise ratio compared to the other observations. In the K2004 and K2005 images, some of the outer shells were not observed due to the smaller field of view and the lower signal-to-noise ratio of the LWS observations.

The position of the nested dust shells between the $\lesssim 3$ yr observation sequences exhibit slight, but measurable radial proper motion. For example, Figure 4 shows the image subtraction residuals between high-pass filtered G2007 and G2004 images. The subtraction residuals demonstrate a $\sim 0\farcs2$–$0\farcs3$ radial proper motion of the eastern and western regions of the first shell beyond the spurs between the G2004 and G2007 images. This is consistent with the positive radial proper motion of the same features between the G2001 and G2004 images as well as the V2016 and S2019 images. The dust emission features in the G2004 and K2004 exhibit a nearly identical morphology, which is consistent with the near-contemporaneous timing of the two observations. The WR 112 nebula in the K2005 image also shows a slight radial expansion from the nebula in the previous K2004 image.

The proper motion of the bright southeast (SE) spur from the 2004 to 2007 images can be traced as it expands into the first nested dust shell in the V2016 and S2019 images. The position of the SE spur is indicated by the "×" marker in Figure 5 (top) on a median-filter subtracted G2007 image. K2004, K2005, G2007, V2016, and S2019 images were median-filter subtracted in order to accentuate the emission from the spur/shell. Radial offsets of the SE spur/shell in the K2004, K2005, G2007, V2016, and S2019 images are measured from the peak location of a Gaussian fit to the emission profile along a radial line cut in the direction of the SE spur (Figure 5, top). The measured SE spur/shell offsets over 2004–2019 are shown in Figure 5 (bottom) and overlaid with a best-fit slope corresponding to a proper motion of 65 ± 8 mas yr^{-1}.

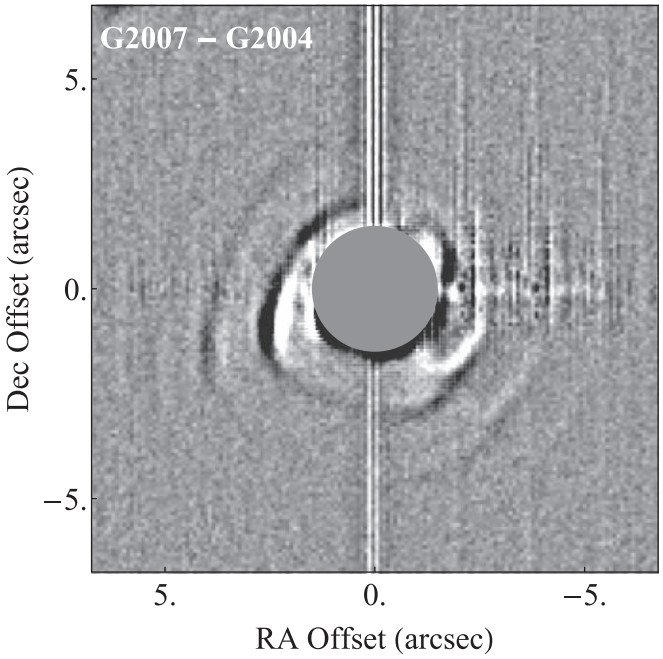

Figure 4. Subtraction residuals of high-pass filtered G2007 and G2004 images. Black and white correspond to positive (G2007) and negative (G2004) emission, respectively. The central region is masked out and the vertical bands extending from the central region are artifacts due to the "hammer effect" (Section 2.2).

Based on the K2004, K2005, and G2007 images, the mean separation distance between the SE spur and the subsequent nested shell (i.e., the distance between the "×" and "○" markers in Figure 5, top) is $1\farcs42$. The full "rotation" period of the repeated shell-like structures can then be estimated from the measured proper motion: $P_{\rm PM} = 21.8^{+3.1}_{-2.4}$ yr. This ∼20 yr period is strengthened by the similar "W"-shaped appearance of the central regions in the G2001 and S2019 images taken 18.4 yr apart.

3.2. Geometric Spiral Model

Marchenko et al. (2002) initially proposed a face-on spiral morphology for WR 112 with dust expanding radially outward like WR 104 and fit a simple Archimedean spiral with an orbital inclination of $i = 38\fdg0 \pm 3\fdg8$. However, this face-on model does not appear to be consistent with the two spurs extending from the central source (Figure 1). Monnier et al. (2007) notably identified these spurs in their high angular resolution (∼20 mas) aperture-masking interferometry observations of WR 112. There are additional linear emission features that deviate from a face-on spiral morphology: for example, in the V2016 image (Figure 2), there are linear features to the northeast that appear to connect the nested shells. These linear features appear in the southwest region of nested shells in the G2004, K2004, K2005, and G2007 images.

Lau et al. (2017) claimed that the segmented dust shells had not moved over decades. However, the sequence of images presented in Figure 2 demonstrate that the dust surrounding

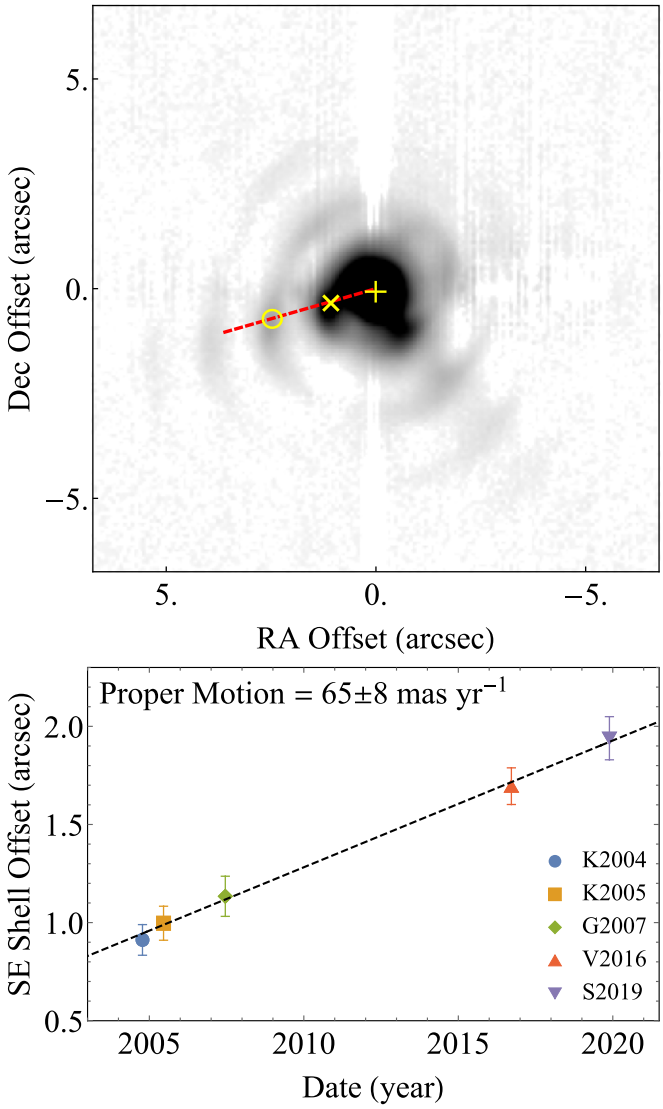

Figure 5. Top: square-root stretch of the median-filter subtracted G2007 image overlaid with the line cut extending from the central core (+) that was used to measure the radial offset of the SE spur/shell (×). The "○" marker indicates the position of the SE spur/shell in the successive shell. Bottom: radial offset plot of the SE spur/shell over five epochs overlaid with the best-fit line whose slope indicates a proper motion of 65 ± 8 mas yr^{-1}.

WR 112 does indeed exhibit radial proper motion, which eliminates the Lau et al. (2017) interpretation of stagnant shells. Here, we revisit the dust morphology of WR 112 and present a revised geometric model.

We fit a simple 3D conical spiral model to WR 112 defined by the separation between successive spiral turns Δr, orbital inclination i, orbital orientation Ω, orbital phase φ, and half-opening angle θ_s. Given the low orbital eccentricity inferred from observations of low-amplitude IR variability from WR 112 (Williams & van der Hucht 2015; Lau et al. 2017), an eccentricity of $e = 0$ is assumed; however, geometric models provide an upper limit estimate of the eccentricity $e \lesssim 0.4$. The model we use provides consistent results with the geometric model utilized by Callingham et al. (2019) and Han et al. (2020) in their morphological analysis of the dusty nebula around Apep.

The basic ($e = 0$) 3D spiral surface of our model, before the size is scaled and the i, Ω, and φ rotation transformations are applied, is defined by the following set of parametric equations along the x, y, and z axes:

$$\begin{aligned} x &= -u\,\mathrm{Sin}(u) + u\,\mathrm{Cos}(u)\mathrm{Cos}(v)\mathrm{Tan}(\theta_s) \\ y &= -u\,\mathrm{Cos}(u) - u\,\mathrm{Sin}(u)\mathrm{Cos}(v)\mathrm{Tan}(\theta_s) \\ z &= -u\,\mathrm{Sin}(v)\mathrm{Tan}(\theta_s) \end{aligned} \quad (1)$$

where $0 < u < 8\pi$ and $0 < v < 2\pi$. The parameters u and v correspond to the angles along the spiral cone surface that are parallel and perpendicular to the orbital plane, respectively. The 8π upper range of u therefore traces four full "windings" of the spiral. The orbital phase $\varphi = 0$ is defined such that at an inclination $i = 90°$, our line of sight is aligned with the opening of the "shock cone" at the apex of the spiral. This $\varphi = 0$, $i = 90°$ spiral orientation corresponds to orbital conjunction in which the WC star is aligned directly behind its OB companion along our line of sight (see Section 3.4).

These parameters are initially fit to the dust emission from the V2016 image, which provides the highest signal-to-noise ratio detection of the extended dust features with minimal imaging artifacts. The models are fit by aligning the 2D projection of the edges of the 3D spiral to the dust emission features in the images (e.g., Figure 6(A)). The G2001, G2004, K2004, K2005, G2007, and S2019 images are then fit by adjusting only the orbital phase φ with the fixed V2016 parameters for Δr, i, Ω, and θ_s. The φ parameters and the dates of the seven observations are used to derive the rotation period of the spiral.

Our fitted model presents the WR 112 nebula as a near edge-on spiral ($i = 100°$) with a wide half-opening angle of $\theta_s = 55°$ where the dust emission corresponds to the edges of the spiral plume. This revised geometry is notably consistent with the edge-on hypothesis suggested by Monnier et al. (2002, 2007). Four full spiral turns of the V2016 spiral model are shown in Figure 6(A) overlaid on the V2016 image, and the spiral model parameters are provided in Table 2. Uncertainties in the model parameters correspond to the upper and lower ranges where the projected spiral edges no longer align with the dust emission from the nebula.

The model fits show that the two spurs extending from the central source are associated with the edges of the spiral plume (Figure 6(A)). Notably, the extended linear emission that connects the nested shells in the V2016 image is reproduced by the projection of the eastern edge of the successive spiral turns. The deviations from circular, azimuthal symmetry are also explained by the high inclination. The model fit to the G2007 image (Figure 6(D)) also reproduces to the observed asymmetric features at a nearly opposite orientation from the V2016 image.

The rotation period of the spiral is $P_{\mathrm{mod}} = 19.4^{+2.7}_{-2.1}$ yr based on a least-squares fit to the seven φ values of the observations with respect to the observation dates. This is consistent with the ∼20 yr period estimate based on the measured proper motion and the ∼1.″4 intervals between the dust arcs (Section 3.1). The date within the seven observations that corresponds to $\varphi = 0$ is $2015.2^{+2.7}_{-2.1}$. Since there is a direct link between the orbital phase of the central dust-forming binary system and the position angle of the dust plume (Monnier et al. 1999; Tuthill et al. 2008), we infer a 19.4 yr orbital period equal to the rotation period for the central binary system of WR 112.

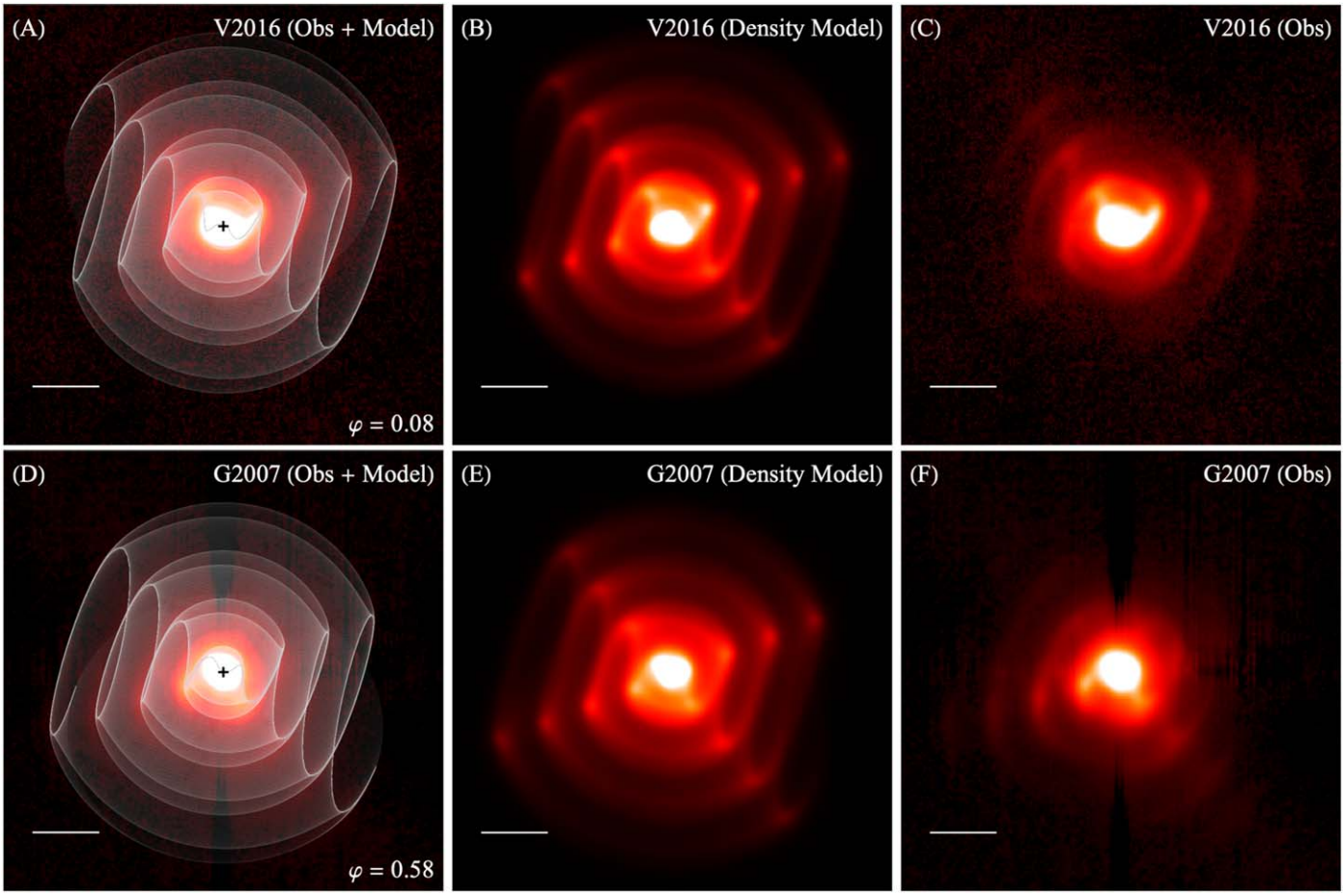

Figure 6. (A) Square-root stretch of the V2016 image of WR 112 overlaid with the V2016 geometric spiral model ($\varphi = 0.08$). The black cross corresponds to the center of the model and is aligned with the emission centroid of the central region. (B) Linear stretch of the dust column density model image at the V2016 epoch. (C) Square-root stretch of the V2016 image. Panels (D)–(F) correspond to the same descriptions as (A)–(C) for the G2007 observation and model ($\varphi = 0.58$). In all panels, north is up and east is left, and the length of the overlaid white lines corresponds to 2″. An animated version of this figure is available that shows (left) the evolution of the density model image (convolved with the VLT/VISIR PSF) over an orbital period from $\varphi = 0$ to 1 with intervals of $\Delta\varphi \approx 0.028$, and (right) a corresponding sequence of V2016, S2019, K2004, and G2007 images with fading transitions that pause for 2 s at the matching model phase. In the both animation panels north is up and east is left, and the length of the white lines corresponds to 2″. The total duration of the animation is 13 s.

(An animation of this figure is available.)

3.3. Model Dust Column Density Image

We produce a 2D dust column density image using the geometry of the fitted 3D spiral in order to compare to the observed dust morphology of the WR 112 nebula. Dust is assumed to be confined to the geometrically thin surface of the 3D conical spiral where the dust density decreases as a function of radius from the central system $n_{\rm d} \propto r^{-2}$. The dust density image is derived from a 2D projection of the 3D geometric spiral, where dust in the spiral is summed along the line of sight in columns consistent with the VISIR pixel scale of $0.045 \times 0\farcs045$.

The V2016 density model image is presented in Figure 6(B), which has also been convolved with the VLT/VISIR NeII_2 PSF that was determined from selected standard stars observed in 2016 (Lau et al. 2017). Four full spiral turns are modeled in the density image, which is consistent with the maximum number of observed spiral turns. The surface brightness of the fourth spiral in the V2016 image is less than 1% of the central region; therefore, the inclusion of additional spiral turns should not significantly alter the density image. It is important to note that the density image effectively models dust emission under the assumption of constant dust temperature and does not reproduce the exact observed dust emission profile from the WR 112 nebula, where dust temperature decreases as a function of radius from the central system ($T_{\rm d} \propto r^{-0.4}$; Marchenko et al. 2002; Lau et al. 2017). However, it is still informative to compare the morphology and column density projection effects from the model image to the observed dust emission.

The morphology and limb brightening in the V2016 density model closely reproduces the dust emission in the V2016 image (Figures 6(B) and (C)). The observed nested shell-like emission beyond the central spurs indeed corresponds to the limb brightened edges of the 3D spiral model. Notably, the locations of high column density "corners" in the density image where the spiral curves and aligns with our line of sight is consistent with regions of locally enhanced dust emission in the V2016 image.

A comparison of the G2007 density model and image (Figures 6(E) and (F)) shows the same close agreement. The timing of the G2007 observations notably corresponds to a nearly 180° phase shift from the V2016 observations. The rotated appearance of the spurs and dust emission asymmetries are reproduced by the G2007 density model. The striking

Table 2
WR 112 Geometric Model Results

Parameter	Value
$P_{\rm PM}$	$21.8^{+3.1}_{-2.4}$ yr
$P_{\rm Mod}$	$19.4^{+2.7}_{-2.1}$ yr
Δr	$1\farcs48 \pm 0\farcs10$
θ_s	$55° \pm 5°$
i	$100° \pm 15°$
Ω	$75° \pm 10°$
$\varphi_{\rm G2001}$	0.25 ± 0.14
$\varphi_{\rm G2004}$	0.47 ± 0.11
$\varphi_{\rm K2004}$	0.47 ± 0.11
$\varphi_{\rm K2005}$	0.50 ± 0.11
$\varphi_{\rm G2007}$	0.58 ± 0.11
$\varphi_{\rm V2016}$	0.08 ± 0.08
$\varphi_{\rm S2019}$	0.22 ± 0.11

Note. Summary of the geometric spiral properties of WR 112, in which a circular ($e = 0$) orbit is assumed. $P_{\rm PM}$ and $P_{\rm Mod}$ are the orbital periods derived from the dust proper motion analysis and the geometric model, respectively. The parameters Δr, θ_s, i, and Ω are the separation distances between the successive spiral turns, the half-opening angle of conical spiral, the orbital inclination, and the orbital orientation, respectively. The orbital phase φ fit to the seven different epochs is also given.

resemblance of the density models to the images reinforces our revised interpretation of the WR 112 nebula.

One notable discrepancy between the density model and the observations is that dust emission to the north and south of the central system appears weaker in the observed images. This effect is most noticeable in the northern regions of the outer shells in the V2016 image and the southern regions of the outer shells in the G2007 image (Figures 6(C) and (F)). We note that the "isothermal" density model does not reproduce the effects of radiative heating, which could be responsible for the weaker north and south dust emission. The radiation field from the central binary may indeed be asymmetric given that the dimmed regions of the nebula are aligned with the orbital plane where the impinging radiation may be attenuated by the dense wind collision region between the WC star and its OB companion.

3.4. The Central Binary and Wind Collision Interface

Our revised geometric model of the WR 112 nebula allows us to investigate the configuration of the central WC+OB binary and the shock cone formed by their colliding winds. In Figure 7, we present a face-on projection of the central binary and the colliding-wind interface of WR 112. Due to the dominant momentum of the WC-star wind over the OB-star wind, the "shock cone" opens in the direction of the OB star.

The geometry of the wind interface in Figure 7 is described by the two-wind interaction model by Cantó et al. (1996), which assumes a purely hydrodynamical balance between the winds. In this model, the half-opening angle θ_s of the colliding-wind shock cone can be used to derive the wind momentum ratio $\eta \equiv \frac{\dot{M}_{\rm OB} v_{\rm OB}}{\dot{M}_{\rm WR} v_{\rm WR}}$ as follows (Cantó et al. 1996):

$$\theta_\infty - \tan\theta_\infty = \frac{\pi}{1-\eta}, \tag{2}$$

where $\theta_\infty = \pi - \theta_s$. Given an opening angle of $\theta_s = 55°$, the wind momentum ratio in WR 112 is $\eta \approx 0.13$. The wind

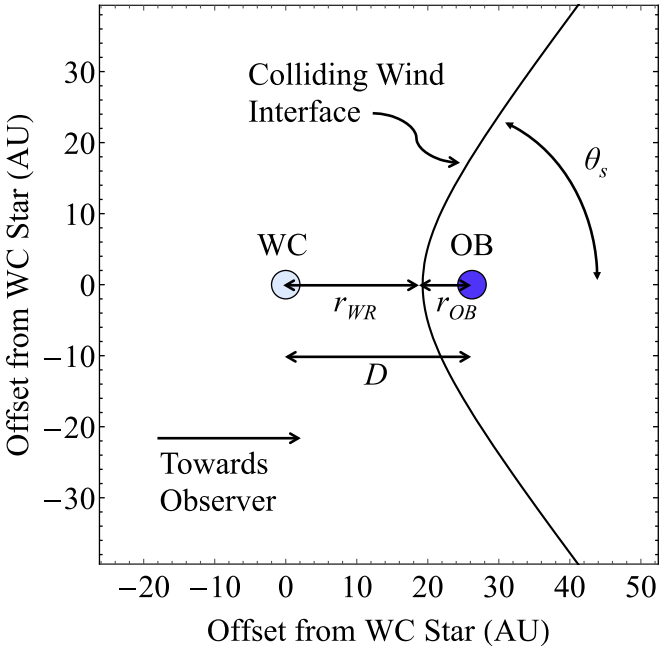

Figure 7. Face-on diagram of the central WR 112 WC+OB binary and the colliding-wind interface with the origin centered on the WC star. The size of the WC and OB star circles are not shown to scale. The orbital separation, D, separation between the WC/OB star and the apex of the shock cone, $r_{\rm WR/OB}$, and the half-opening angle of the shock cone, θ_s, are all shown to scale.

momentum ratio in WR 112 is notably higher than the ratio in face-on pinwheel system WR 104 ($\eta \approx 0.003$; Tuthill et al. 2008), which also exhibits a narrower half-opening angle ($\theta_s \approx 20°$) than WR 112.

The orbital separation and the distances between the WC and OB star and the wind collision region can be estimated from the 19.4 yr orbital period and the wind momentum ratio. Assuming a circular orbit, a WC star mass of 18 $M_\odot$, which is consistent with the mean Galactic WC8 stellar mass derived by Sander et al. (2019), and an OB companion mass of 30 $M_\odot$, the orbital separation of the WR 112 central binary is $D \approx 26$ au. The distances $r_{\rm WR}$ and $r_{\rm OB}$ from the WR and OB star to the wind collision region can then be derived from the following relation by Usov (1991):

$$r_{\rm WR} = D\frac{1}{1+\eta^{1/2}},\ r_{\rm OB} = D\frac{\eta^{1/2}}{1+\eta^{1/2}}. \tag{3}$$

It follows from Equation (3) that the separation distances between the WR and OB star from the wind collision front are $r_{\rm WR} \approx 19$ au and $r_{\rm OB} \approx 7$ au. The separation distances as well as the colliding-wind interface are shown to scale in Figure 7.

Lastly, it is important to note that the orbital motion of the central binary will lead to "aberrations" of the apex of the shock interface (Parkin & Pittard 2008), which is not incorporated in the shock cone geometry shown in Figure 7, as its effects in WR 112 are negligible. The effect of these aberrations can be characterized by a skew angle μ between the binary axis and the symmetric axis of the colliding-wind interface: $\tan(\mu) = (v_{\rm orb}/v_\infty)$, where $v_{\rm orb}$ is the orbital speed of the binary (Parkin & Pittard 2008). For the central binary of WR 112, $v_{\rm orb} \approx 40$ km s^{-1} and $v_\infty \approx 1230$ km s^{-1}, which demonstrates that the skew angle $\mu \approx 1\fdg9$ is indeed small.

3.5. Revised WR 112 Distance Estimate

Previous distance estimates toward WR 112 are highly uncertain and range from 1.3 to 4.15 kpc (Nugis et al. 1998; van der Hucht 2001) due to the large interstellar extinction ($A_v = 12.24$; van der Hucht 2001), its dusty nebula, and luminous neighbor (Wallace et al. 2002). A recent study by Rate & Crowther (2020), who perform a Bayesian analysis on Gaia DR2 parallaxes to 383 Galactic WR stars with priors based on H II regions and dust extinction, obtains a distance of $d = 3.16^{+2.06}_{-1.07}$ kpc. However, Rate & Crowther (2020) flag WR 112 for exhibiting a large negative parallax and high astrometric excess noise > 1 mas.

Similar to previous studies of WR 104 (Tuthill et al. 2008; Soulain et al. 2018), we can estimate the distance to WR 112 by assuming the observed dust expansion velocity is consistent with the terminal velocity of the WC wind. Based on the model period $P_{\rm Mod}$ and the intervals between the spiral turns from the geometric model Δr, the model-derived dust expansion rate is $\Delta r/P_{\rm Mod} = 76^{+12}_{-10}$ mas yr^{-1}. Given the $v_\infty = 1230 \pm 260$ km s^{-1} terminal wind velocity measured from the FWZI of the 5696 Å C III line in the WHT/ISIS spectrum (Figure 3), we derive a distance to WR 112 of $d = 3.39^{+0.89}_{-0.84}$ kpc.

This method of deriving WC dustar distances is notably challenged by the discovery of discrepant WC wind and dust expansion velocities in the WC dustar Apep, where the spectroscopically measured line-of-sight WR wind velocity is a factor of ~4 higher than the observed dust expansion velocity (Callingham et al. 2019, 2020; Han et al. 2020). Apep's velocity discrepancy is attributed to a rapidly rotating WR star that exhibits a slow equatorial wind, where dust forms via wind collision with its companion, and a fast polar wind, where dust formation is absent (Callingham et al. 2019, 2020). Assuming spin–orbit alignment, the spectroscopically measured fast wind is indeed consistent with our line-of-sight alignment toward Apep's pole given the near face-on inclination of its orbit ($i \approx 25°$; Han et al. 2020). Apep's viewing geometry notably differs from WR 112's, which we interpret as near edge-on. Therefore, even if the WC star in WR 112 exhibits a discrepant equatorial and polar wind, its spectrum would be dominated by the same equatorial wind along our line of sight that condenses into dust via colliding winds from its companion. We therefore claim that the distance estimate method of equating the measured WC wind terminal velocity to the observed dust expansion velocity is valid for WR 112.

3.6. Revisiting Dust Production Properties from WR 112

In this section, we revisit the dust production properties of WR 112 based on our proper motion analysis, revised distance estimate, and new geometric model. In order to determine the dust properties, we fit a two-component optically thin dust emission model to an extinction-corrected ISO/SWS 2.2–27.5 μm spectrum of WR 112 (Figure 8). Reddening by interstellar extinction is corrected using the ISM extinction law derived by Chiar & Tielens (2006) normalized to the visual extinction measured toward WR 112 of $A_V = 11.03$.[14] Initially, a single component dust model was attempted but resulted in an unsatisfactory fit due to the broad shape of the SWS spectrum. We note that the measured flux density from the SWS observations, which were taken in 1996 February, are consistent within ~20% of the ground-based V2016 (Lau et al. 2017) and S2019 mid-IR photometry. This supports the interpretation of WR 112 as a continuous dust producer with minimal variability in dust production.

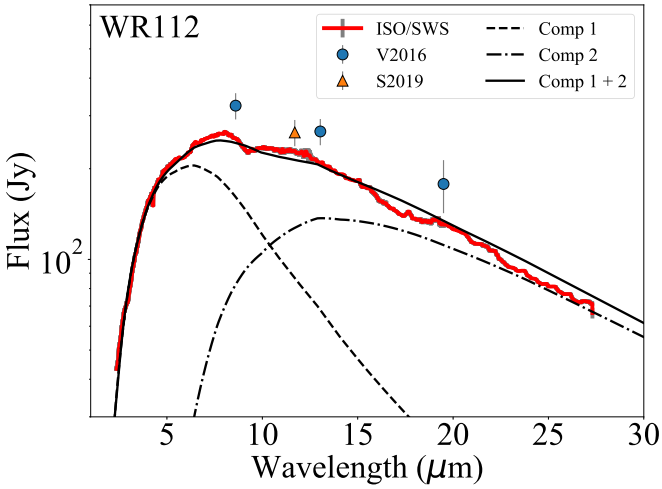

Figure 8. Extinction-corrected ISO/SWS spectrum of WR 112 taken in 1996 February (red line) overlaid with the dereddened *N*-band photometry from V2016 (Lau et al. 2017; blue circles) and S2019 (orange triangle) and the best-fit two-component dust emission model. The emission from components 1 and 2 are shown as the dashed and dotted–dashed lines, respectively, and the total combined model emission is shown as the solid black line.

We produce dust emission models using `DustEM`, a numerical tool that computes the dust emission in the optically thin limit heated by an input radiation field with no radiative transfer (Compiègne et al. 2011). Our two-component dust model technique is identical to the WC dustar spectral energy distribution (SED) analysis by Lau et al. (2020). The two components are treated as circular dust rings with different radii heated radiatively by a central heating source, where the inner dust ring (r_1) attenuates the radiation heating the outer dust ring (r_2). Since the circumstellar material around WC dustars is believed to be composed of amorphous carbon dust (Cherchneff et al. 2000), amorphous carbon grains with optical properties described by Zubko et al. (1996) and Compiègne et al. (2011) are adopted for the `DustEM` model. We use a grain size distribution with radii ranging from $a = 0.1$–1.0 μm and a number density distribution proportional to $n(a) \propto a^{-3}$. This grain size distribution is consistent with the ~0.5–1.0 μm grain radii estimated in the WR 112 nebula by previous studies (Chiar & Tielens 2001; Marchenko et al. 2002).

The luminosity of the central system is not well characterized given the high interstellar extinction. We therefore adopt a total system luminosity of $L_* = 4.0 \times 10^5$ $L_\odot$ in agreement with the mean WC8 stellar luminosity determined by Sander et al. (2019) and assume that the WC star dominates the radiative heating. A Potsdam Wolf–Rayet Star model atmosphere (Gräfener et al. 2002; Sander et al. 2012, 2019) with an effective temperature of $T_* = 50{,}000$ K and "transformed" radius of 7.9 $R_\odot$ was adopted for the radiation field of the WR 112 heating source, which is consistent with the values derived from the spectral pseudo-fit to the dusty WC8 system WR 53 by Sander et al. (2019).

Our best-fit two-component model provides dust component distances of $r_1 = 140^{+40}_{-50}$ au and $r_2 = 910^{+240}_{-350}$ au corresponding to components 1 and 2, respectively. The dust temperature of the two components are $T_{\rm d1} = 830^{+150}_{-70}$ K and $T_{\rm d2} = 300^{+100}_{-40}$ K,

[14] This is consistent with the extinction derived by van der Hucht (2001) where $A_v \approx 1.1 A_V$.

Table 3
WR 112 Distance and Dust Model Results

Parameter	Value
d	$3.39^{+0.89}_{-0.84}$ kpc
r_1	140^{+40}_{-50} au
r_2	910^{+240}_{-350} au
T_{d1}	830^{+150}_{-70} K
T_{d2}	300^{+100}_{-40} K
L_{IR}	$(6.6^{+0.3}_{-0.1})^{+3.9}_{-2.9} \times 10^4\ L_\odot$
M_{d1}	$(1.4^{+1.0}_{-1.0})^{+0.9}_{-0.6} \times 10^{-6}\ M_\odot$
M_{d2}	$(8.2^{+4.7}_{-4.9})^{+4.9}_{-3.6} \times 10^{-5}\ M_\odot$
$\dot{M}_d$	$(2.7^{+1.0}_{-1.3})^{+1.6}_{-1.2} \times 10^{-6}\ M_\odot\ \mathrm{yr}^{-1}$
χ_C (4π steradians)	$(6.5^{+2.3}_{-3.0})^{+0.8}_{-0.9}\%$
χ_C ($\pm\theta_s$ equatorial band)	$\sim 8\%$

Note. Summary of the distance d and dust model results of WR 112, where the following values are adopted: $v_{exp} = 1230$ km s^{-1}, $\dot{M} = 1.1 \times 10^{-4}\ M_\odot\ \mathrm{yr}^{-1}$ (Monnier et al. 2002). The radius, temperature, and mass of the model components 1 and 2 are given as $r_{1/2}$, $T_{d1/d2}$, and $M_{d1/d2}$, respectively. L_{IR} is the total IR luminosity of both dust components. The dust production rate $\dot{M}_d$ and the dust condensation fraction of available carbon the WC wind χ_C are derived using the expansion derived by v_{exp}^{PM}, M_{d1}, and r_1. The first and second set of uncertainties provided for L_{IR}, M_{d1}, M_{d2}, $\dot{M}_d$, and χ_C correspond to the 1σ uncertainties from the SED model fit and the WR 112 distance estimate, respectively. The distance to WR 112 does not impact the values derived for $r_{1/2}$ and $T_{d1/d2}$, and therefore only the SED model-fit uncertainties are shown for these quantities.

and the total integrated IR luminosity of both components is $L_{IR} = 6.6^{+0.3}_{-0.1} \times 10^4\ L_\odot$. High spatial resolution 2.2 μm observations of WR 112 by Ragland & Richichi (1999) revealed an inner dust radius of 31 mas, which corresponds to a size of $\sim$110 au at a distance $d = 3.39$ kpc. The resolved inner dust radius and our model-derived component 1 radius are therefore in close agreement. We also note that component 1 dominates the emission at 2.2 μm (Figure 8) and is thus consistent with the emitting dust component resolved by Ragland & Richichi (1999).

From the two-component model, we derive dust masses of $M_{d1} = 1.4^{+1.0}_{-1.0} \times 10^{-6}\ M_\odot$ and $M_{d2} = 8.2^{+4.7}_{-4.9} \times 10^{-5}\ M_\odot$ for components 1 and 2, respectively. Using the dust distances and masses, the dust production rate can be approximated by

$$\dot{M}_d \sim \frac{M_d\ v_{exp}}{r}. \quad (4)$$

We adopt a conservative estimate of the dust production rate based only on the dust mass and the distance to component 1, as cooler and more extended dust may contribute to the dust mass determined for component 2. Assuming the dust expansion velocity, v_{exp}, is equal to the terminal wind velocity of the WC star $v_\infty = 1230$ km s^{-1} (See Section 3.5), the dust production rate based on component 1 is $\dot{M}_d = 2.7^{+1.0}_{-1.3} \times 10^{-6}\ M_\odot\ \mathrm{yr}^{-1}$. The WR 112 dust model results are summarized in Table 3. We note that only the SED model-fitting uncertainties are provided in the text of this section, whereas Table 3 lists both the model-fitting uncertainties and the uncertainties due to our distance estimate.

The total mass-loss rate of the WC wind in WR 112 derived from its thermal radio emission by Monnier et al. (2002) is $1.1 \times 10^{-4}\ M_\odot\ \mathrm{yr}^{-1}$, which has been rescaled to our revised $d = 3.39$ kpc distance. By assuming a carbon mass fraction of 40% in WC winds (Sander et al. 2012, 2019), we estimate a carbon dust mass condensation fraction in WR 112 of $\chi_C = 6.5^{+2.3}_{-3.0}\%$. Note that this is the condensation fraction for the total mass-loss rate of WR 112 over 4π steradians. However, the region over which the WC wind can contribute to dust formation is constrained to the equatorial angular band within $\pm\theta_s$ of the orbital plane (Tuthill et al. 2008). For $\theta_s = 55°$, this equatorial angular band is 82% of the 4π steradians subtended by the WC wind in WR 112. Therefore, $\sim$8% of the carbon by mass from the WC wind in this equatorial band condenses to dust. These results provide strong evidence that dust can form efficiently in the colliding winds of WC binaries.

4. Discussion

4.1. Reconciling WR 112 Nonthermal Radio Variability

With the revised geometric spiral model of WR 112, we can resolve lingering uncertainties about the nature of WR 112 posed by previous radio observations (e.g., Monnier et al. 2002). WR 112 exhibited highly variable nonthermal radio emission, which is difficult to reconcile with a face-on geometry (Monnier et al. 2002, 2007). Nonthermal radio emission arises from particle acceleration in the shock collision zone between the winds of the WC and OB star; however, the nonthermal radio emission can be absorbed by the dense, ionized stellar winds of the WC and OB star (Eichler & Usov 1993). Variability in the nonthermal radio emission can therefore arise from the orbital motion of a near edge-on central binary due to changes in the optical depth along the line of sight to the wind collision zone.

The variable and highly absorbed nonthermal radio emission from WR 112 was revealed by Chapman et al. (1999), who measured a 2.38 GHz flux density of $F_{2.38\mathrm{GHz}} = 3.8$ mJy in 1997, which was a factor of 10 greater than the expected 2.38 GHz flux density based on a purely thermal emission model and a 8.64 GHz flux density measurement of $F_{8.64\,\mathrm{GHz}} = 0.68$ mJy in 1995 by Leitherer et al. (1997). Monnier et al. (2002) showed that WR112 was in a radio bright state between 1999 September and 2000 February, when the 1.425 GHz flux density was measured to be $\sim$2.5 mJy, while the 1.38 GHz flux density measurement by Chapman et al. (1999) in 1997 provided an upper limit of < 1.1 mJy. Notably, radio observations of WR 112 by Monnier et al. (2002) implied a shallower slope between the 2.38 and 1.38 GHz flux density measurements by Chapman et al. (1999), which suggests a lower free–free opacity in the Monnier et al. (2002) observations.

In Figure 9, we show three orbital phases of the 3D spiral model and the projection of the colliding-wind interface corresponding to different dates between 1995 and 2000. The projected shock cone shown in Figure 9 is the 3D surface of the shock interface shown in Figure 7 and is analogous to the conic surface $\tilde{C}$ in Eichler & Usov (1993). Note that the shock cone surface in Figure 9 does not incorporate the influence of the binary orbital motion since this effect on the skew angle of the shock cone is negligible (See Section 3.4).

Based on our geometric model, our line of sight toward WR 112 was aligned with the interior of the shock cone between 1995 and 1997, which correspond to orbital phases $\varphi \sim 0$ and 0.1, respectively (Figures 9(A) and (B)). Nonthermal radio variability is expected in this orientation, in which optically thick winds from the OB companion can

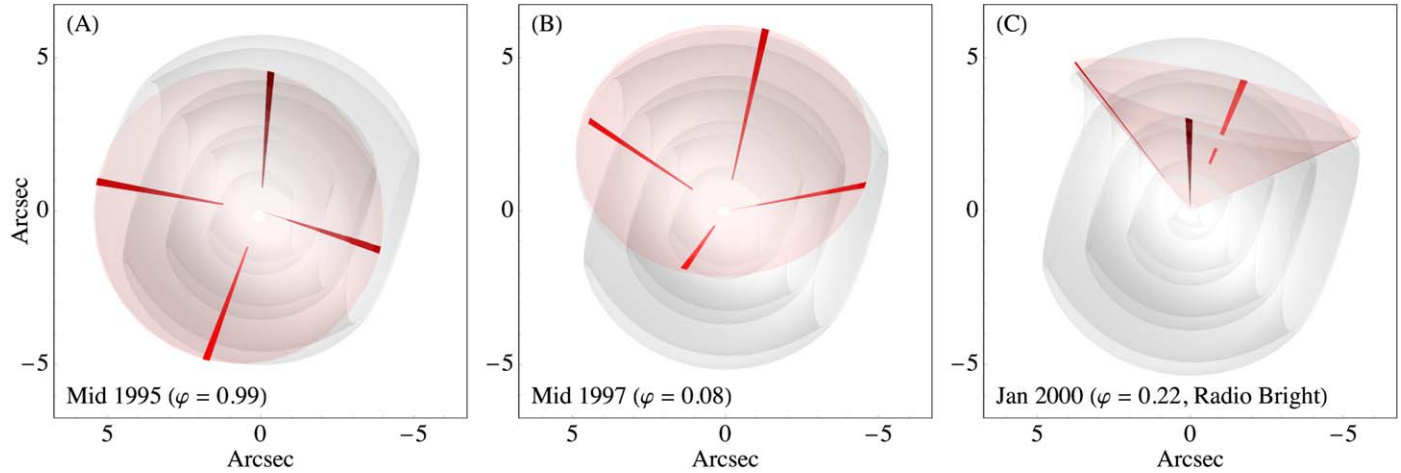

Figure 9. 3D surface model of WR 112 (gray) overlaid with the projection of the colliding-wind interface of the central binary (red) at our predicted viewing angle in (A) mid 1995, (B) mid 1997, and (C) 2000 January. In each panel, red bands are overlaid on the surface of the shock cone to help illustrate the orientation and geometry. WR 112 was observed in a radio bright state between 1999 September and 2000 February (Monnier et al. 2002).

obscure the shock collision zone (Eichler & Usov 1993; Dougherty et al. 2003). During the radio bright state between late 1999 and early 2000, our model at 2000 January is consistent with an orbital phase of $\varphi = 0.22$, which is near quadrature. Nonthermal radio emission models of a WR+OB colliding-wind system by Dougherty et al. (2003) demonstrate that attenuation from free–free opacity is weakest near quadrature. At this phase where the WC and OB star are aligned parallel to the plane of the sky, our line of sight toward the nonthermal emission region at the apex of the shock interface is less obscured by the stellar winds from both the WR star and its companion. The revised near edge-on geometry of the WR 112 system is therefore consistent with the observed radio variability.

The subsequent quadrature in which WR 112 should have exhibited another radio bright state would have occurred in 2010, which is half an orbital phase (∼10 yr) after the observed radio bright state in late 1999–early 2000. Interestingly, the radio light curve of WR 112 presented by Yam et al. (2015) reveals an 8.4 GHz emission peak from ∼2010 to 2011, which is consistent with our model prediction; however, the flux density measured by Yam et al. (2015) during this peak is a factor of ∼3 less than the 8.46 GHz emission ($F_{8.46\,\mathrm{GHz}} = 4.07$) reported by Monnier et al. (2002) in 2000 February. WR 112's next radio bright state should occur during the following quadrature expected in ∼2020–2021.

4.2. WR 112 and WC Dustar Diversity

WR 112 exhibits one of the highest dust production rates of the known WC dustars, which range from $\sim 10^{-10}$ to 10^{-6} $M_\odot\,\mathrm{yr}^{-1}$ (Lau et al. 2020). Despite their contrasting orbital and colliding-wind shock properties, WR 112 exhibits a dust production rate comparable to one of the heaviest known dust makers WR 104 ($\sim 4 \times 10^{-6}$ $M_\odot\,\mathrm{yr}^{-1}$; Lau et al. 2020). A comparison between WR 112 and WR 104 therefore highlights the range of the WC binary orbital parameters that exhibit high dust production rates ($\sim 10^{-6}$ $M_\odot\,\mathrm{yr}^{-1}$). To provide a comparative benchmark, this dust production rate exceeds the total measured dust input from the AGB stars in the Small Magellanic Cloud ($\sim 9 \times 10^{-7}$ $M_\odot\,\mathrm{yr}^{-1}$; Boyer et al. 2012). Both WR 112 and WR 104 host late-type WC+OB binaries with near circular orbits. However, WR 104 is a near face-on system with an orbital separation of ∼2 au and a relatively narrow colliding-wind half-opening angle $\theta_s \approx 20°$ (Tuthill et al. 2008), while WR 112 is a near edge-on system with an orbital separation of ∼20 au and a wide colliding-wind half-opening $\theta_s = 55°$.

Since dust formation is linked to the wind interaction with the binary companion, it is interesting to compare the inferred properties of the OB companions in WR 112 and WR 104. Harries et al. (2004) propose that WR 104 hosts an OB companion that exhibits a mass-loss rate of 6×10^{-8} $M_\odot\,\mathrm{yr}^{-1}$ with an assumed wind velocity of 2000 km s^{-1}. Based on the mass-loss rate and wind velocity of the WC star in WR 112 and the wind momentum ratio $\eta \approx 0.13$ derived from its observed opening angle (Equation (2)), we estimate a mass-loss rate of $\sim 8 \times 10^{-6}$ $M_\odot\,\mathrm{yr}^{-1}$ for the OB companion with an assumed wind velocity of 2000 km s^{-1}. This high mass-loss rate would be consistent with an early O-type supergiant (e.g., Muijres et al. 2012). Companions with such high mass-loss rates may be necessary to enable dust formation in systems with large orbital separations/periods such as WR 112, WR 48a ($P_{\mathrm{orb}} = 32.5$ yr; Williams et al. 2012), and Apep ($P_{\mathrm{orb}} \sim 100$ yr; Han et al. 2020). Both WR 48a and Apep indeed host companions that exhibit high mass-loss rates (Zhekov et al. 2014; Callingham et al. 2020). Interestingly, WR 112, WR 48a, and Apep exhibit WR emission lines consistent with a WC8 star.

The range of orbital separations exhibited by WC dustars and possible trends with their spectral subtypes highlight the importance of investigating the relation between their dust formation efficiency and stellar and orbital properties. The longer orbital period of WR 112 relative to other heavy WC dust makers with ∼1 yr periods like WR 104 also highlights the diversity of WC systems that exhibit high dust formation rates and bolsters their likely role as significant sources of dust in the interstellar medium (Lau et al. 2020).

5. Conclusions

We have presented a multi-epoch morphological analysis of the complex geometry of the dusty circumstellar environment formed by the colliding-wind binary WR 112. Our analysis utilized high resolution *N*-band imaging observations of WR 112 taken over almost a 20 yr baseline with Gemini

North/OSCIR, Gemini South/T-ReCS, Keck I/LWS, VLT/VISIR, and Subaru/COMICS (Figures 1 and 2). WR 112's changing dust morphology is consistent with a nearly edge-on 3D conical spiral with a wide opening angle that appears to rotate due to persistent dust formation from a central colliding-wind WC binary with a ∼20 yr orbital period. The motion of the dust, however, is not along the spiral but is radial since dust forms and propagates in the changing direction of the shock cone between the WC star and its companion.

The observed dust emission morphology and the dust column density model image derived from the revised geometry show a close match (Figure 6), which supports our revised interpretation of the WR 112 nebula geometry. Our geometric model and the inferred ∼20 yr orbital period provides us with insight on the orbital configuration of the central binary and the shock cone produced by the wind collision.

We revisited the distance estimate and dust production properties of WR 112 with this revised geometric model and estimate high dust production rates and dust condensation efficiency. With a dust production rate of $\sim 3 \times 10^{-6}\, M_{\odot}\, \mathrm{yr}^{-1}$, WR 112 is among the most prolific dust makers of all known WC dustars and highlights their impact as significant dust producers in the interstellar medium.

The nearly edge-on interpretation of WR 112 reconciles inconsistencies highlighted by previous observations of variable nonthermal radio emission from the wind collision zone. Continued radio observations and future work on the correlation between the mid-IR dust morphology and radio light curve would therefore provide valuable insight on the wind collision region and the properties of the stellar winds. Additionally, future observations utilizing very long baseline interferometry may be able to reveal the morphology of nonthermal emission (e.g., Dougherty et al. 2005; Sanchez-Bermudez et al. 2019).

Given to its IR brightness, resolvable extended emission, and high dust formation rate, WR 112 presents a unique laboratory to investigate dust formation and wind collision dynamics in colliding-wind binaries. State-of-the-art hydrodynamic simulations and 3D radiative transfer models (e.g., Lamberts et al. 2012; Hendrix et al. 2016; Soulain et al. 2018; Calderón et al. 2020) of WR 112 would deepen our understanding of such phenomena. WR 112's relatively extended emission compared to the nebulae around shorter period dusty WC systems also provides a valuable reference for interpreting the morphologies of other dust-forming colliding-wind binaries. Lastly, we emphasize the importance of multi-epoch high spatial resolution mid-IR observations for pursuing these studies. Mid-IR instrumentation on future observatories such as the Tokyo Atacama Observatory (Miyata et al. 2010), 30 m class telescopes, and the James Webb Space Telescope will be crucial for unraveling the nature of dust formation in these efficient dust factories.

R.M.L. thanks D. Calderón, A. Lamberts, S.V. Marchenko, J.D. Monnier, T. Onaka, G. Rate, C..P. Russell, and R. Schödel for the valuable discussion on colliding winds in WC binaries and observations of WR 112. We thank the anonymous referee for the insightful comments and suggestions that have improved the clarity and quality of this work. R.M.L. also thanks T. Fujiyoshi and the Subaru Observatory staff for supporting our Subaru/COMICS observations of WR 112. R.M.L. acknowledges the Japan Aerospace Exploration Agency's International Top Young Fellowship. A.F.J.M. is grateful for financial aid from NSERC (Canada). Based in part on observations collected at the European Organisation for Astronomical Research in the Southern Hemisphere under ESO program 097.D-0707(A). Some of the data presented herein were obtained at the W. M. Keck Observatory, which is operated as a scientific partnership among the California Institute of Technology, the University of California, and the National Aeronautics and Space Administration. The Observatory was made possible by the generous financial support of the W. M. Keck Foundation. The authors wish to recognize and acknowledge the very significant cultural role and reverence that the summit of Maunakea has always had within the indigenous Hawaiian community. We are most fortunate to have the opportunity to conduct observations from this mountain. Based in part on data collected at Subaru Telescope, which is operated by the National Astronomical Observatory of Japan. Based in part on observations obtained at the international Gemini Observatory, a program of NOIRLab, which is managed by the Association of Universities for Research in Astronomy (AURA) under a cooperative agreement with the National Science Foundation on behalf of the Gemini Observatory partnership: the National Science Foundation (United States), National Research Council (Canada), Agencia Nacional de Investigación y Desarrollo (Chile), Ministerio de Ciencia, Tecnología e Innovación (Argentina), Ministério da Ciência, Tecnologia, Inovações e Comunicações (Brazil), and Korea Astronomy and Space Science Institute (Republic of Korea). Based in part on observations with ISO, an ESA project with instruments funded by ESA Member States (especially the PI countries: France, Germany, the Netherlands, and the United Kingdom) and with the participation of ISAS and NASA. Based in part on observations in the service observing program of the WHT, operated on the island of La Palma by the Isaac Newton Group of Telescopes in the Spanish Observatorio del Roque de los Muchachos of the Instituto de Astrofísica de Canarias. This research made use of Astropy,[15] a community-developed core Python package for Astronomy (Astropy Collaboration et al. 2013, 2018).

Facilities: VLT(VISIR), Subaru(COMICS), Gemini South (T-ReCS), Keck I(LWS), Gemini North(OSCIR), ISO(SWS), WHT(ISIS).

ORCID iDs

Matthew J. Hankins https://orcid.org/0000-0001-9315-8437
Michael E. Ressler https://orcid.org/0000-0001-5644-8830
Itsuki Sakon https://orcid.org/0000-0001-7641-5497
Joel Sanchez-Bermudez https://orcid.org/0000-0002-9723-0421
Ian R. Stevens https://orcid.org/0000-0001-7673-4340
Peredur M. Williams https://orcid.org/0000-0002-8092-980X

References

Astropy Collaboration, Price-Whelan, A. M., Sipőcz, B. M., et al. 2018, AJ, 156, 123
Astropy Collaboration, Robitaille, T. P., Tollerud, E. J., et al. 2013, A&A, 558, A33
Boyer, M. L., Srinivasan, S., Riebel, D., et al. 2012, ApJ, 748, 40
Calderón, D., Cuadra, J., Schartmann, M., et al. 2020, MNRAS, 493, 447

[15] http://www.astropy.org

Callingham, J. R., Crowther, P. A., Williams, P. M., et al. 2020, MNRAS, 495, 3323
Callingham, J. R., Tuthill, P. G., Pope, B. J. S., et al. 2019, NatAs, 3, 82
Cantó, J., Raga, A. C., & Wilkin, F. P. 1996, ApJ, 469, 729
Chapman, J. M., Leitherer, C., Koribalski, B., et al. 1999, ApJ, 518, 890
Cherchneff, I., Le Teuff, Y. H., Williams, P. M., et al. 2000, A&A, 357, 572
Chiar, J. E., & Tielens, A. G. G. M. 2001, ApJL, 550, L207
Chiar, J. E., & Tielens, A. G. G. M. 2006, ApJ, 637, 774
Cohen, M., & Kuhi, L. V. 1976, PASP, 88, 535
Cohen, M., Walker, R. G., Carter, B., et al. 1999, AJ, 117, 1864
Compiègne, M., Verstraete, L., Jones, A., et al. 2011, A&A, 525, A103
Crowther, P. A. 2007, ARA&A, 45, 177
Crowther, P. A., De Marco, O., & Barlow, M. J. 1998, MNRAS, 296, 367
Currie, M. J., Berry, D. S., Jenness, T., et al. 2014, in ASP Conf. Series 485, Astronomical Data Analysis Software and Systems XXIII, ed. E. Manset & P. Forshay (San Francisco, CA: ASP), 391
Cutri, R. M., Skrutskie, M. F., van Dyk, S., et al. 2003, yCat, 2246
De Buizer, J., & Fisher, R. 2005, in Proc. ESO Workshop, High Resolution Infrared Spectroscopy in Astronomy, ed. H. U. Käufl (Garching: ESO), 84
de Graauw, T., Haser, L. N., Beintema, D. A., et al. 1996, A&A, 315, L49
Dougherty, S. M., Beasley, A. J., Claussen, M. J., et al. 2005, ApJ, 623, 447
Dougherty, S. M., Pittard, J. M., Kasian, L., et al. 2003, A&A, 409, 217
Eichler, D., & Usov, V. 1993, ApJ, 402, 271
Gehrz, R. D., & Hackwell, J. A. 1974, ApJ, 194, 619
Gräfener, G., Koesterke, L., & Hamann, W.-R. 2002, A&A, 387, 244
Han, Y., Tuthill, P. G., Lau, R. M., et al. 2020, MNRAS, submitted (arXiv:2008.05834)
Harries, T. J., Monnier, J. D., Symington, N. H., et al. 2004, MNRAS, 350, 565
Hendrix, T., Keppens, R., van Marle, A. J., et al. 2016, MNRAS, 460, 3975
Jones, B., & Puetter, R. C. 1993, Proc. SPIE, 1946, 610
Kataza, H., Okamoto, Y., Takubo, S., et al. 2000, Proc. SPIE, 4008, 1144
Kessler, M. F., Steinz, J. A., Anderegg, M. E., et al. 1996, A&A, 500, 493
Lagage, P. O., Pel, J. W., Authier, M., et al. 2004, Msngr, 117, 12
Lamberts, A., Dubus, G., Lesur, G., et al. 2012, A&A, 546, A60
Lau, R. M., Eldridge, J. J., Hankins, M. J., et al. 2020, ApJ, 898, 74
Lau, R. M., Hankins, M. J., Schödel, R., et al. 2017, ApJL, 835, L31
Leitherer, C., Chapman, J. M., & Koribalski, B. 1997, ApJ, 481, 898
Marchenko, S. V., & Moffat, A. F. J. 2007, in ASP Conf. Series 367, Massive Stars in Interactive Binaries, ed. N. St-Louis & A. F. J. Moffat (San Francisco, CA: ASP), 213
Marchenko, S. V., & Moffat, A. F. J. 2017, MNRAS, 468, 2416
Marchenko, S. V., Moffat, A. F. J., Vacca, W. D., et al. 2002, ApJL, 565, L59
Massey, P., & Conti, P. S. 1983, PASP, 95, 440
Miyata, T., Sako, S., Nakamura, T., et al. 2010, Proc. SPIE, 7735, 77353P
Monnier, J. D., Greenhill, L. J., Tuthill, P. G., et al. 2002, ApJ, 566, 399
Monnier, J. D., Tuthill, P. G., & Danchi, W. C. 1999, ApJL, 525, L97
Monnier, J. D., Tuthill, P. G., Danchi, W. C., et al. 2007, ApJ, 655, 1033
Muijres, L. E., Vink, J. S., de Koter, A., et al. 2012, A&A, 537, A37
Murakawa, K., Suto, H., Tamura, M., et al. 2004, PASJ, 56, 509
Nugis, T., Crowther, P. A., & Willis, A. J. 1998, A&A, 333, 956
Okamoto, Y. K., Kataza, H., Yamashita, T., et al. 2003, Proc. SPIE, 4841, 169
Parkin, E. R., & Pittard, J. M. 2008, MNRAS, 388, 1047
Ragland, S., & Richichi, A. 1999, MNRAS, 302, L13
Rate, G., & Crowther, P. A. 2020, MNRAS, 493, 1512
Sanchez-Bermudez, J., Alberdi, A., Schödel, R., et al. 2019, A&A, 624, A55
Sander, A., Hamann, W.-R., & Todt, H. 2012, A&A, 540, A144
Sander, A. A. C., Hamann, W.-R., Todt, H., et al. 2019, A&A, 621, A92
Shortridge, K. 1993, in ASP Conf. Series 52, Astronomical Data Analysis Software and Systems II, ed. R. J. Hanisch et al. (San Francisco, CA: ASP), 219
Sloan, G. C., Kraemer, K. E., Price, S. D., & Shipman, R. F. 2003, ApJS, 147, 379
Soulain, A., Millour, F., Lopez, B., et al. 2018, A&A, 618, A108
Tuthill, P. G., Monnier, J. D., & Danchi, W. C. 1999, Natur, 398, 487
Tuthill, P. G., Monnier, J. D., Lawrance, N., et al. 2008, ApJ, 675, 698
Usov, V. V. 1991, MNRAS, 252, 49
van der Hucht, K. A. 2001, NewAR, 45, 135
van der Hucht, K. A., Morris, P. W., Williams, P. M., et al. 1996, A&A, 315, L193
Wallace, D. J., Moffat, A. F. J., & Shara, M. M. 2002, in ASP Conf. Series 260, Interacting Winds from Massive Stars, ed. A. F. J. Moffat & N. St-Louis (San Francisco, CA: ASP), 407
Williams, P. M., & van der Hucht, K. A. 2015, in International Workshop on Wolf-Rayet Stars, ed. W.-R. Hamann et al. (Postdam: Universitätsverlag Potsdam), 275
Williams, P. M., van der Hucht, K. A., Pollock, A. M. T., et al. 1990, MNRAS, 243, 662
Williams, P. M., van der Hucht, K. A., & Thé, P. S. 1987, A&A, 182, 91
Williams, P. M., van der Hucht, K. A., van Wyk, F., et al. 2012, MNRAS, 420, 2526
Yam, J. O., Dzib, S. A., Rodríguez, L. F., et al. 2015, RMxAA, 51, 35
Zhekov, S. A., Gagné, M., & Skinner, S. L. 2014, ApJ, 785, 8
Zubko, V. G. 1998, MNRAS, 295, 109
Zubko, V. G., Mennella, V., Colangeli, L., et al. 1996, MNRAS, 282, 1321